Imaging and tracking single plasmonic nanoparticles in 3D background-free with four-wave mixing interferometry

Paola Borri, Naya Giannakopoulou, George Zoriniants, Iestyn Pope, Francesco Masia, et al.

Paola Borri, Naya Giannakopoulou, George Zoriniants, Iestyn Pope, Francesco Masia, Peter Watson, Wolfgang Langbein, "Imaging and tracking single plasmonic nanoparticles in 3D background-free with four-wave mixing interferometry," Proc. SPIE 10894, Plasmonics in Biology and Medicine XVI, 108940Z (7 March 2019); doi: 10.1117/12.2507618

SPIE.

Event: SPIE BiOS, 2019, San Francisco, California, United States

Imaging and tracking single plasmonic nanoparticles in 3D background-free with four-wave mixing interferometry

Paola Borri[a], Naya Giannakopoulou[a], George Zoriniants[a], Iestyn Pope[a], Francesco Masia[a], Pete Watson[a], and Wolfgang Langbein[b]

[a]Cardiff University School of Biosciences, Museum Avenue, Cardiff CF10 3AX, United Kingdom
[b]Cardiff University School of Physics and Astronomy, The Parade, Cardiff CF24 3AA, United Kingdom

ABSTRACT

We present a four-wave mixing interferometry technique recently developed by us, whereby single non-fluorescing gold nanoparticles are imaged background-free even inside highly heterogeneous cellular environments, owing to their specific nonlinear plasmonic response. The set-up enables correlative four-wave mixing/confocal fluorescence imaging, opening the prospect to study the fate of nanoparticle-biomolecule-fluorophore conjugates and their integrity inside cells. Beyond imaging, the technique features the possibility to track single particles with nanometric position localisation precision in 3D from rapid single-point measurements at 1 ms acquisition time, by exploiting the optical vortex field pattern in the focal plane of a high numerical aperture objective lens. These measurements are also uniquely sensitive to the particle in-plane asymmetry and orientation. The localisation precision in plane is found to be consistent with the photon shot-noise, while axially it is limited to about 3 nm by the nano-positioning sample stage, with an estimated photon shot-noise limit of below 1 nm. As a proof-of-principle, the axial localisation is exploited to track single gold nanoparticles of 25 nm radius while diffusing across aqueous pockets in a dense agarose gel, mimicking a relevant biological environment.

Keywords: Nonlinear optical microscopy, nano-plasmonics, four-wave-mixing, single particle tracking

1. INTRODUCTION

Imaging and tracking single nanoparticles using optical microscopy are powerful techniques with many applications in biology, chemistry, and material sciences. Despite significant advances, imaging single particles in a scattering environment (such as, for example, biological cells) as well as localizing objects with nanometric position precision remains challenging. Applied methods to achieve contrast and specificity against backgrounds in heterogeneous environments often rely on the detection of fluorescence emission. However, fluorophores are single-quantum emitters and are thus only capable of emitting a certain maximum number of photons per unit time due to the finite duration of their excited-state lifetime. Moreover, they are prone to photobleaching and associated phototoxicity.

Alternatively to using fluorescent emitters, single particle imaging and tracking can be implemented with non-fluorescing metallic nanoparticles (NPs) that exhibit strong light scattering and absorption at the localised surface plasmon resonance (LSPR). This signal is photostable, and the achievable photon fluxes are governed by the incident photon fluxes and the NP optical extinction cross-section. Numerous techniques have been shown in the literature to image and track metallic NPs, including bright-field microscopy,[1] dark-field microscopy,[2] differential interference contrast (DIC),[3] interferometric scattering microscopy (iSCAT),[4] and photothermal imaging[5] (for a review see also Ref. 6). Generally, however, all these techniques are not background-free, and rapid tracking of small NPs in 3D with high precision in a scattering environment remains challenging.

In 2009, we invented, patented and demonstrated four-wave mixing (FWM) imaging interferometry, triply-resonant to the LSPR, as a very selective, photostable and background-free method to detect single small (<

Further author information: Send correspondence to borrip@cf.ac.uk

Plasmonics in Biology and Medicine XVI, edited by Tuan Vo-Dinh, Ho-Pui A. Ho, Krishanu Ray, Proc. of SPIE
Vol. 10894, 108940Z · © 2019 SPIE · CCC code: 1605-7422/19/$18 · doi: 10.1117/12.2507618

40 nm) gold NPs (AuNPs) inside biological cells.[7,8] In 2012, we showed phase-sensitive time-resolved detection of the resonant FWM from a single AuNP which brought new insights on the physical origin of this nonlinearity.[9,10] More recently, we developed a latest generation of the technique comprising a new FWM detection modality that can determine the position of a single AuNP in the 15-30 nm radius range with shot-noise limited precision better than 20 nm in plane and 1 nm axially from scanless single-point background-free acquisition on a 1 ms time scale, by exploiting optical vortices of tightly focused light.[11] The technique is also uniquely sensitive to particle asymmetries down to 0.5% ellipticity, corresponding to a single atomic layer of gold.

Here, we review some of these results and show a proof-of-principle application where we track single gold nanoparticles of 25 nm radius while diffusing and jumping across aqueous pockets in a dense agarose gel, mimicking a relevant biological environment.

2. EXPERIMENTAL SET-UP

A sketch of the FWM set-up is shown in Fig. 1. We use a train of femtosecond optical pulses which is split into three beams (called pump, probe and reference), all having the same center optical frequency, resulting in a triply degenerate FWM scheme.

Optical pulses of 150 fs duration and repetition rate $\nu_L = 80$ MHz, centered at $\lambda = 550$ nm are provided by the signal output of an optical parametric oscillator (Newport/Spectra Physics, OPO Inspire HF 100), pumped by the frequency-doubled output of a femtosecond Titanium:Sapphire laser (Newport/Spectra Physics, Mai Tai HP). The OPO signal output beam is linearly polarised horizontally (H) with respect to the laboratory reference system, and passes through a prism pulse compressor used to precompensate the chirp introduced by all the optics in the beam path, in order to achieve Fourier-limited pulses of 150 fs duration at the sample. After the pulse compressor, the train of optical pulses passes through a $\lambda/2$ waveplate which rotates the linear polarisation by 45°. The beam then enters a polarising beam splitter (PBS_1) and is split into an H-polarised transmitted beam and a vertically (V) polarised reflected beam of equal intensity, acting as probe and pump pulses respectively. The V polarised pump beam is absorbed by the AuNP at the LSPR, with an intensity temporally modulated by an acousto-optic modulator (AOM_1). AOM_1 is driven at the carrier frequency $\nu_1 = 83$ MHz with a square-wave amplitude modulation of frequency $\nu_m = 0.4$ MHz. The change in the NP optical properties induced by the pump is resonantly probed by the probe beam, arriving at an adjustable delay time τ after the pump pulse (using a motorized delay line into the pump beam path). The probe optical frequency is upshifted via a second AOM (AOM_2) which is driven with a constant amplitude at $\nu_2 = 82$ MHz. The first order diffraction of the AOMs are used for both pump and probe pulses (which are in turn upshifted by ν_1 and ν_2 respectively). The zero order diffraction of AOM_2 is used as a frequency-unshifted reference beam, for interferometric heterodyne detection as detailed below. Pump and probe beams, cross-linearly polarised, are recombined onto a second polarising beam splitter (PBS_2) and are then reflected by a non-polarising beamsplitter (BS_1, 80:20 Transmission:Reflection) into a pair of waveplates ($\lambda/2$ and $\lambda/4$) used to transform pump and probe into circularly polarised beams at the sample plane. The recombined beams are further reflected by a dichroic beam splitter (DBS) into the right port of a commercial inverted microscope stand (Nikon Ti-U). Notably, DBS allows us to couple beams of different wavelengths into the microscope when performing other experiments, such as for example coherent antiStokes Raman scattering microscopy.[12] Here, it was used for correlative FWM confocal fluorescence microscopy, as described in section 3.1. The sample can be positioned and moved with respect to the focal volume of the microscope objective by scanning an xyz sample stage with nanometric position precision (MadCityLabs NanoLP200). The microscope objective was either a 100× magnification oil-immersion objective of 1.45 NA (Nikon CFI Plan Apochromat lambda series) or a 60× magnification water-immersion objective of 1.27 NA (Nikon CFI Plan Apochromat lambda series). Pump and probe pulses of fields $\mathbf{E}_1$ and $\mathbf{E}_2$, respectively, recombined into the same spatial mode and focused onto the sample by the high NA microscope objective, generate a FWM field proportional to $\mathbf{E}_1\mathbf{E}_1^*\mathbf{E}_2$. The FWM field is collected together with the probe in reflection (epi-direction) by the same microscope objective, transmitted by the beam splitter (BS_1) used to couple the incident beams onto the microscope, and recombined in a second beam splitter (BS_2) with the reference pulse field of adjustable delay (using a motorized delay line into the reference beam path). Note that pump and probe pulses should have the same chirp in the beam path so that they can be equally pre-compensated, and be Fourier limited at the sample. For this purpose, appropriate glass blocks where inserted in the beam path. Furthermore, since the reference

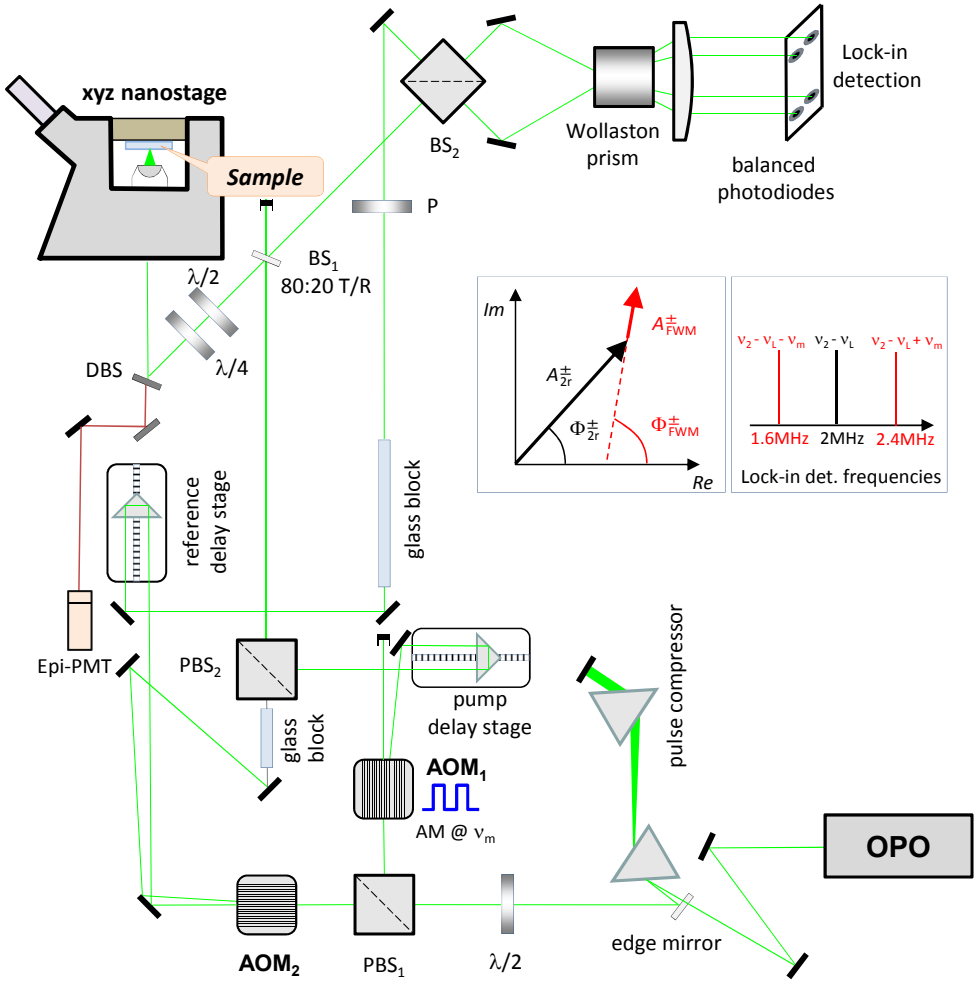

Figure 1. Sketch of the FWM set-up (see also text). Optical pulses are provided by the signal output of an Optical Parmetric Oscillator (OPO). Pump and probe beams are created using a polarising beam splitter (PBS_1). Pump pulses are amplitude-modulated (AM) at the frequency $\nu_m = 0.4\,MHz$ and probe pulses are frequency shifted by $\nu_2 = 82\,MHz$, using acousto-optical modulators (AOMs). Pulses are recombined via a second polarising beam splitter (PBS_2) and coupled into an inverted microscope equipped with a high NA microscope objective. Pump and probe beams are adjusted to be circularly polarized at the sample by $\lambda/4$ and $\lambda/2$ waveplates. Circular polarisations are transformed into horizontal and vertical linear polarisation by the same waveplates and both components are simultaneously detected through their interference with a frequency-unshifted reference linearly polarised at 45°. Inset: amplitude (A) and phase (Φ) of the reflected probe and FWM field, measured by a multi-channel lock-in, where +(-) refers to the co(cross) polarised component relative to the incident circularly polarized probe. The various frequencies simultaneously detected by the multi-channel lock-in amplifier are also shown.

beam does not travel through the microscope objective, glass blocks of known group-velocity dispersion were added to the reference beam path, in order to match the chirp introduced by the microscope optics and thus maximize the interference between the reflected FWM field and the reference field at the detector.

The interference between the epi-collected FWM field and the reference field is detected by two pairs of balanced silicon photodiodes (Hamamatsu S5973-02). As a result of the amplitude modulation of the pump at ν_m and the frequency shift of the probe at ν_2, this interference gives rise to a beat note at ν_2 with two sidebands at $\nu_2 \pm \nu_m$, and replica separated by the repetition rate ν_L of the pulse train. A multi-channel lock-in amplifier (Zürich Instruments HF2LI) enables the simultaneous detection of the carrier at $\nu_2 - \nu_L = 2\,MHz$ and the sidebands at $\nu_2 \pm \nu_m - \nu_L = 2 \pm 0.4\,MHz$. This heterodyne scheme thus discriminates the FWM field from

pump and probe pulses. Note that the separation of the side bands is much higher than the lock-in amplifier detection bandwidth (inverse of twice the pixel dwell time) in the 1 kHz range, i.e. the detected signals have no significant cross talk. Via the in-phase (Re) and in-quadrature (Im) components for each detected frequency, amplitude and phase of the probe field reflected by the sample $\mathbf{E}_{2\mathrm{r}}$ (detected at $\nu_2 - \nu_\mathrm{L}$) and of the epi-detected FWM field $\mathbf{E}_\mathrm{FWM}$ (at $\nu_2 \pm \nu_\mathrm{m} - \nu_\mathrm{L}$) are measured (see sketches in Fig. 1).

A key point of the technique is the use of a dual-polarisation balanced detection. The reflected probe and FWM fields collected by the same microscope objective travel backwards through the same waveplates, such that the probe reflected by a planar surface returns V polarized in the laboratory system. The reference beam is polarised at 45 degree (using the polariser P) prior to recombining with the epi-detected signal via the non-polarizing beamsplitter BS_2. A Wollaston prism vertically separates H and V polarizations for each arm of the interferometer after BS_2. The two pairs of balanced photodiodes then provide polarization resolved detection, detecting the current difference (for common-mode noise rejection) of the V and H polarised interferometer arms. In turn, this corresponds to detecting the co- and cross-circularly polarised components of $\mathbf{E}_{2\mathrm{r}}$ and $\mathbf{E}_\mathrm{FWM}$ relative to the incident circularly polarized probe, having amplitudes (phases) indicated as $A^{\pm}_{2\mathrm{r}}$ and $A^{\pm}_\mathrm{FWM}$ ($\Phi^{\pm}_{2\mathrm{r}}$ and $\Phi^{\pm}_\mathrm{FWM}$) in the sketch in Fig. 1 where + (-) refers to the co (cross) polarised component.

3. IMAGING SINGLE NANOPARTICLES BACKGROUND-FREE INSIDE CELLS

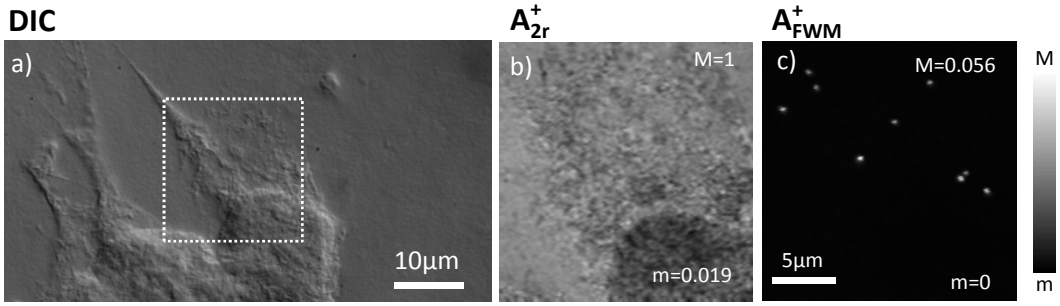

Figure 2. Background-free FWM imaging of single 20 nm radius gold NPs in fixed HeLa cells. The heterogeneity of the cell is shown with differential interference contrast (a) and reflectometry (amplitude of the reflected probe field, $A^+_{2\mathrm{r}}$) (b). (c) shows the FWM field amplitude A^+_FWM. FWM was acquired with a pump-probe delay time of 0.5 ps, pump (probe) power at the sample of 30 μW (15 μW), 2 ms pixel dwell time, using a 1.45 NA oil-immersion microscope objective. FWM is shown as a maximum intensity projection over a 5 μm axial-stack, while the reflection is on a single x, y plane (scanning the sample position).

As explained in our previous works,[9,10] FWM excitation and detection in our technique can be understood as a pump-probe scheme. The resonant absorption of a short pump pulse induces the formation of a hot electron gas in the metal which changes the NP dielectric constant. The corresponding change in the NP transmission and scattering is resonantly probed by the probe pulse, resulting in the FWM field. The heterodyne detection geometry described in section 2 provides interferometric detection free from incoherent (e.g. fluorescence) backgrounds, and distinguishes the FWM field from the scattered pump and probe fields, even though they are all having the same center wavelength (degenerate FWM). By varying the delay time between pump and probe pulses, the electron dynamics can be time-resolved, revealing the time scale of the thermalisation between the electrons and the lattice of the metal ($\sim$ 1 ps) and the subsequent thermalisation of the NP with the surrounding medium ($>$ 100 ps).[9,10] This dynamics enables us to distinguish the electronic NP response from instantaneous coherent backgrounds and/or long-lived photothermal effects. As a result, we can achieve completely background-free FWM imaging of single AuNPs even in scattering and fluorescing cellular environments.

To exemplify this point, Fig. 2 shows fixed HeLa cells (the oldest and most commonly used human cell line derived from cervical cancer cells) that have internalized AuNPs of 20 nm radius (as per protocol described in Ref. 11), imaged with FWM using a 1.45 NA oil-immersion objective. High-resolution differential interference contrast (DIC) microscopy was available in the same instrument, with wide-field illumination via an oil condenser of 1.35 NA and detection with a Canon EOS 40D camera attached to the left port of the microscope stand. As

described in section 2, the set-up enables simultaneous interferometric detection of the reflected probe field and FWM field. Fig. 2 shows the DIC image of a group of HeLa cells on which reflection and FWM imaging was performed in the region highlighted by the dashed frame. The reflection image (amplitude of the reflected probe field, A^+_{2r}) shown in Fig. 2 correlates with the cell contour seen in DIC and shows a spatially varying contrast due to thickness and refractive index inhomogeneities in the sample. Even with a particle diameter as large as 40 nm, AuNPs are not distinguished from the cellular contrast in DIC or in the reflection image. On the contrary, the FWM field amplitude A^+_{FWM} shown in Fig. 2 as a maximum intensity projection over a 5 μm axial-stack is background-free (throughout the z stack) and clearly indicates the location of single AuNPs in the cell.

3.1 Correlative FWM/Confocal fluorescence imaging

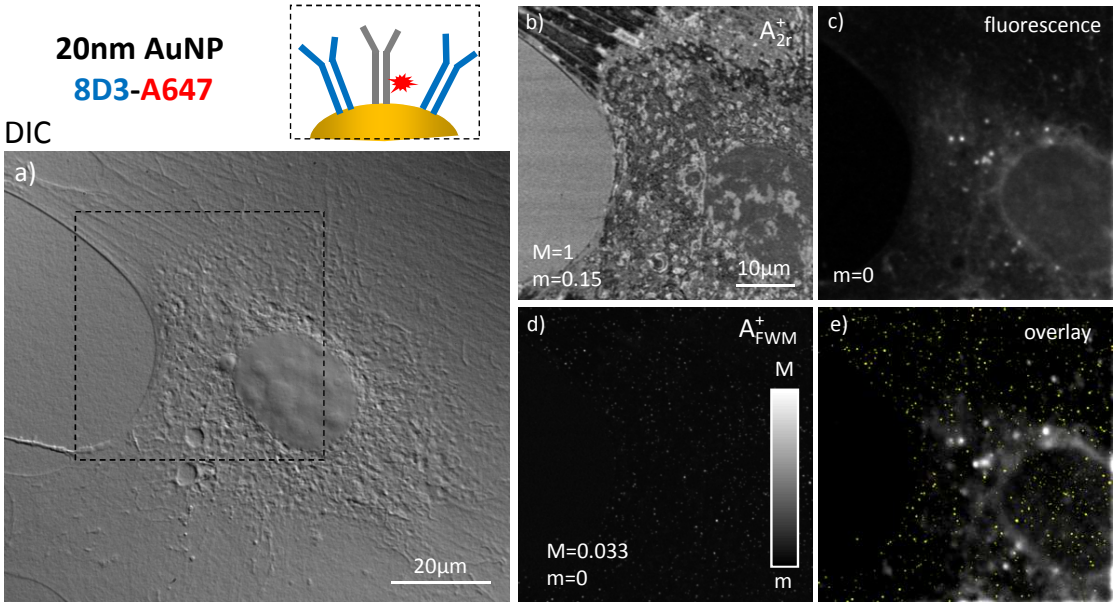

Figure 3. Fixed 3T3-L1 cells that have internalized gold NPs of 10nm radius imaged by (a) differential interference contrast (DIC) microscopy, (b) co-circularly polarised reflection amplitude (A^+_{2r}), (c) confocal epi-fluorescence, (d) co-circularly polarised FWM amplitude (A^+_{FWM}). The top sketch shows the AuNP fluorophore construct consisting of unspecific goat-antirabbit antibodies fluorescently labelled with Alexa647 (A647) as well as unlabelled 8D3 mouse-specific antibodies covalently bound to the AuNP surface. Amplitude scales from m to M are indicated (for confocal fluorescence M=1.37 $\times$ 10^6 (photoelectrons/sec)). FWM was acquired with pump-probe delay time of 0.5 ps, pump (probe) power at the sample of 60 μW (30 μW), 0.4 ms pixel dwell time, pixel size in plane of 63 nm and z-stacks over 3μm in 500 nm z-steps. FWM is shown as a maximum intensity projection over the z-stack, while the reflection and fluorescence images are on a single xy plane (scanning the sample position). e) is a false color overlay of the FWM (yellow) and fluorescence images in c) and d) respectively, brightness and contrast enhanced for visualization purposes.

FWM acquisition can be performed simultaneously with confocal fluorescence microscopy for correlative co-localisation analysis. Confocal epi-fluorescence detection was implemented in the same microscope set-up (see also sketch in Fig. 1), by conjugating the sample plane onto a confocal pin-hole of adjustable opening in front of a photomultiplier detector (Hamamatsu H10770A-40). Excitation occurred via the same laser beam used for FWM. Fluorescence was collected via the same objective (in this case 1.45 NA oil-immersion lens) and spectrally separated using a dichroic beam splitter (DBS) for pick-up and a bandpass filter transmitting in the 600-700 nm wavelength range in front of the photomultiplier.

An example of this simultaneous FWM/fluorescence acquisition is shown Fig. 3 where 3T3-L1 cells (a fibroblast-like mouse cell line) have been loaded with commercially available AuNPs of 10nm radius (InnovaCoat GOLD 20OD Conjugation Kit, Innova Biosciences) which had a proprietary protective surface coat onto which proteins or antibodies can be covalently bound. Unspecific goat-antirabbit antibodies fluorescently labelled with

Alexa647 (Innova Biosciences) as well as unlabelled 8D3 mouse-specific antibodies were bound to these AuNPs in equal mixture, following the manufacture protocol. 8D3 recognises the transferrin receptor (TfR) protein, of importance in the regulation and distribution of circulating iron in cells, via clathrin-mediated endocytosis which is also relevant in current cancer management strategies.[13] Following incubation with the AuNPs for 15min, 3T3-L1 cells were washed in phosphate-buffered saline (PBS) at pH 7.4 and then fixed in 3% paraformaldehyde for 10min at room temperature, washed 3 times in PBS pH 7.4 and then mounted onto glass slides using Mowiol mounting medium. They were then imaged with DIC, reflection, FWM and simultaneous confocal fluorescence.

The co-circularly polarized reflection image (A^{+}_{2r}) in Fig. 3b correlates with the cell contour seen in DIC in the region highlighted by the dashed frame, and shows a spatially varying contrast due to thickness and refractive index inhomogeneities in the sample. Epi-fluorescence in Fig. 3c correlates with the cell morphology seen in DIC and the reflection image. However, while we were expecting to detect the emission from the fluorophore label Alexa647 in the fluorescence image under our excitation and detection conditions, we find that the signal is dominated by cellular autofluorescence, especially significant near the cell nucleus, by comparison with unlabelled control cells (not shown). Moreover, preliminary data (not shown) indicate that even in regions outside the cell, hence not dominated by the cellular autofluorescence background, the fluorescence intensity from the AuNP-Alexa67 construct is undetectable. The co-circularly polarised FWM amplitude A^{+}_{FWM} shown in Fig. 3d is a maximum intensity projection over a 3μm z-stack and clearly indicates the location of single AuNPs in the cell. FWM imaging is background-free (throughout the z-stack) despite the significant scattering and autofluorescing cellular contrast seen in Fig. 3a,b,c. Fig. 3e shows a false color overlay of the FWM and fluorescence image.

The question as to whether the Alexa647 fluorophore is bleached, to the extent of making it undetectable against the background even outside the cell, or is actually not attached to the AuNP and thus does not correlate with the AuNP location observed in FWM, will be the subject of future work. Notably, the ability to perform correlative FWM/fluorescence microscopy exemplified in Fig. 3 opens the prospect to ask this important question, and more in general to study the intracellular fate of AuNP-biomolecule-fluorophore conjugates. These are widely utilised in cell biology, and are often assumed to remain intact, as opposed to the fluorescently labelled molecule being unbound and actually trafficking independently from the AuNP. With our correlative FWM/fluorescence technique we will be able to investigate the integrity of these constructs by unambiguously visualising the location of AuNPs in a way that was not possible before.

4. TRACKING SINGLE NANOPARTICLES

Two important features of the FWM interferometry technique that we have developed enable us to achieve single particle localisation with nanometric precision in 3D from rapid single-point measurements at 1 ms acquisition time. These are i) reflection (epi) collection geometry (as opposed to transmission), and ii) dual circular-polarisation detection (see also sketch in Fig. 1). Feature i) enables us to localise the axial position of a single AuNP. This is because in the epi-geometry a change in the particle axial position results in a change of the optical path length of the reflected wave. The coherent interferometric detection of the phase (Φ^{+}_{FWM}) of the reflected FWM field thus directly encodes the particle axial coordinate (which is not possible in transmission geometry). Feature ii) allows for the detection of the particle in-plane coordinates. Due to the high numerical aperture of the microscope objective and the vectorial nature of the light field, there is a significant cross-circularly polarised field component that forms an optical vortex of l=2 topological charge in the focal plane (i.e. it has an amplitude which is zero in the focus centre, increases proportional to the square of the radius away from the centre, and a phase changing with twice the in-plane polar angle). Owing to the presence of such an optical vortex field pattern, an off-centre in-plane particle position results in a non-zero FWM field component cross-circularly polarised (relative to the input probe circular polarisation), with an amplitude (A^{-}_{FWM}) and phase (Φ^{-}_{FWM}) measured at a single point (i.e. scanless) which encode the direction and position of the particle. Fig. 4a shows our calculations of A^{-}_{FWM} and Φ^{-}_{FWM} for a 1.45 NA oil immersion objective, as described in Ref. 11, exhibiting the l=2 optical vortex field pattern, and a sketch of how the in-plane polar coordinates of the particle can be derived from A^{-}_{FWM} and Φ^{-}_{FWM} respectively.

Notably, we found in the experiments that a tiny deviation from perfect spherical shape of the NP in-plane results in a cross-circularly polarised component. This was evident when measuring AuNPs immobilised onto a glass surface. We were able to model our experimental findings by assuming an ellipsoid nanoparticle in the dipole

limit, and in turn calculating the pump-induced change of the particle polarizability probed by the probe field and interferometrically detected through its interference with a mode-matched reference field, as a function of the NP position in the sample focal plane (for more details see Ref. 11). These calculations, and their comparison with experiments on a nominally spherical 30 nm radius NP are shown in Fig. 4a. From the calculations, we find that the non-zero value of A^{-}_{FWM} in the focus centre scales linearly with the particle ellipticity in-plane, and that the value of Φ^{-}_{FWM} in the focus depends on the particle orientation angle. We can explain the experimental results shown in Fig. 4a by assuming NP semi-axes of $a = 30.135$ nm and $b = c = 30$ nm along the x, y, and z axes in the particle reference system, and the longer axis being rotated in plane relative to the x-axis in laboratory system by about 150 degrees. It is remarkable that an asymmetry of only 0.5% in aspect ratio, or about one atomic layer of gold, manifests as a significant perturbation of the cross-polarized field patterns compared to the spherical case.

When NPs are not immobilized onto a surface but are freely rotating (a more relevant scenario for particle-tracking applications), we can expect that the acquired field components time averaged over a sufficiently long acquisition time would no longer be affected by the particle asymmetry since this is averaged upon rotation.

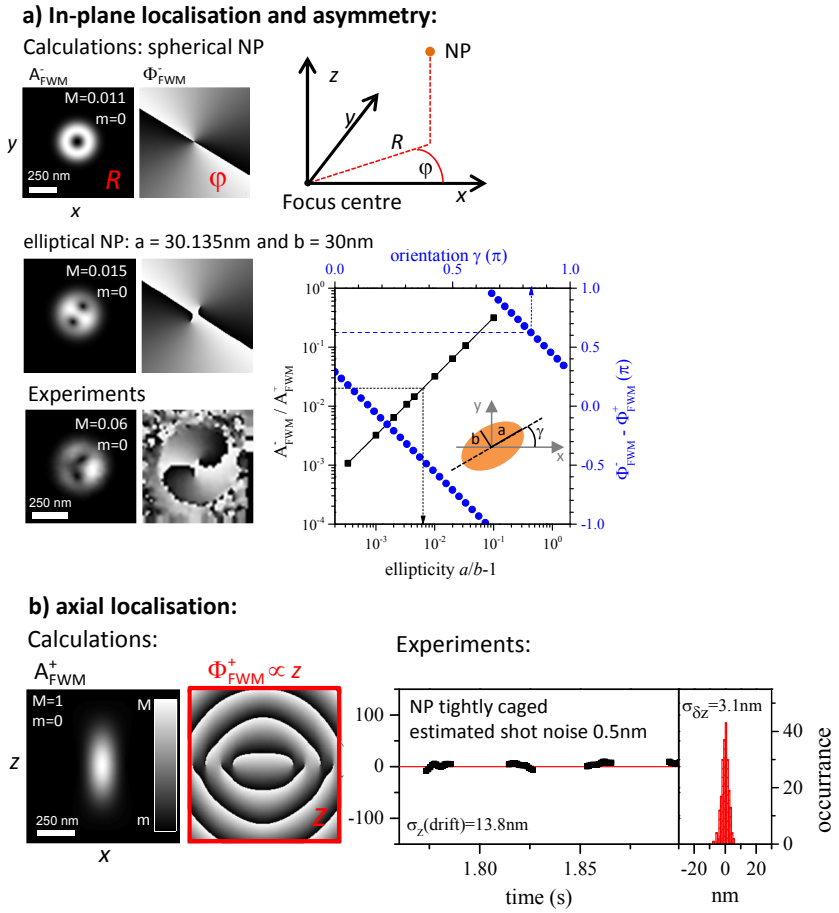

Figure 4. a(top): Calculation of the field distribution in the focal plane elucidating the concept of in-plane localisation via the l = 2 optical vortex in the cross-circularly polarised FWM field amplitude (A^{-}_{FWM}) and phase (Φ^{-}_{FWM}), for a 1.45 NA objective (see text). a(middle): Experiments and calculations of the effect of NP asymmetry, assuming an ellipsoid nanoparticle in the dipole limit with semiaxis a and b in-plane (see text). b: Axial (z) localisation via the phase of the reflected FWM field. Photon shot-noise precision at 1 ms acquisition on a 25 nm radius gold NP is estimated to be 0.5 nm. Measured localisation is practically limited by noise in the sample stage (3 nm rms) and drifts (for more details see also Ref. 11).

For this purpose we investigated single AuNPs of 25 nm radius embedded in a dense (5% w/v) agarose gel in water and measured using an index-matched 1.27 NA water-immersion objective. Specifically, we looked at NPs that were freely rotating but enclosed in a tight pocket of the agar network, resulting in a negligible average translation during the measurement time. In this case, we were able to demonstrate that the NP position retrieval based on our FWM read-out resulted in a localisation with 16 nm precision in plane and 3 nm axially from rapid single-point measurements at 1 ms acquisition time (for more details see Ref. 11). The precision in plane was found to be consistent with the estimated photon shot-noise, while axially it is limited by the nano-positioning sample stage. The estimated shot-noise limited axial localization precision was actually below 1 nm (see Fig. 4b and Ref. 11).

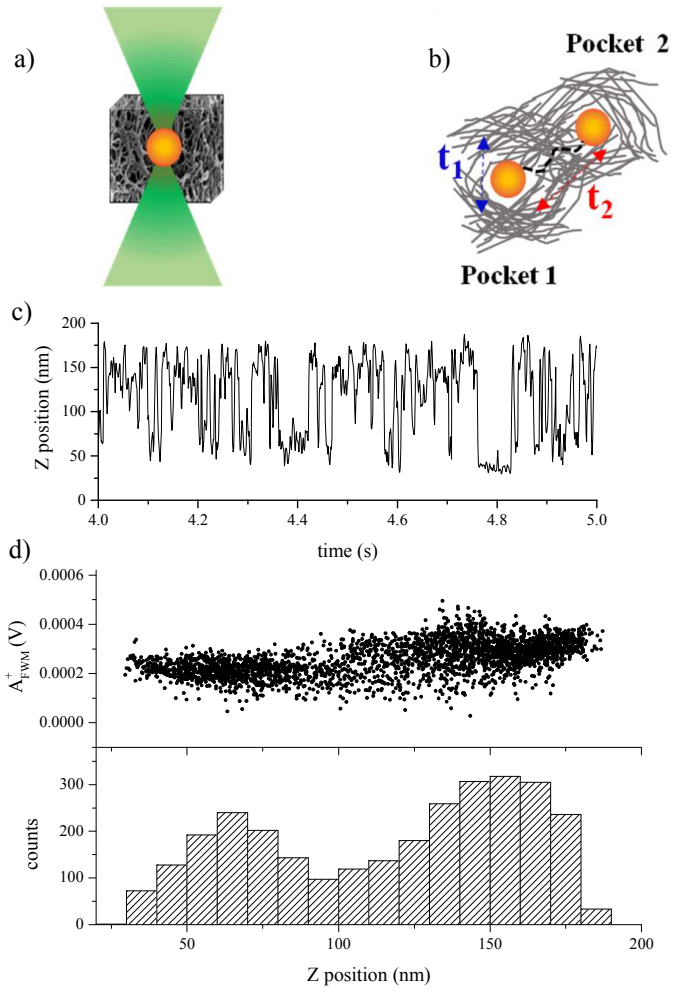

Figure 5. a) Sketch of the investigated sample: a AuNP inside a dense (5% w/v) agarose gel is illuminated by a tightly focused laser beam and is tracked axially over time, without moving the beam focus, via the measurement of Φ^+_{FWM}. b) Sketch of the observed diffusion behavior: the NP undergoes constraint diffusion inside a pocket in the agarose gel (with characteristic time t_1) and 'jumps' across two pockets (with characteristic time t_2). c) Time trace of the AuNP axial position from $z = (\partial z/\partial\Phi)\Phi^+_{\mathrm{FWM}}$. d) Histogram of the AuNP axial position, alongside the corresponding amplitude of the co-circularly polarised field A^+_{FWM}, indicating that the NP jumps over two pockets in the agarose gel, separated by about 80 nm. Data were acquired with 1 ms dwell time over a time window of 3 s, with pump (probe) power 7.5 (3.75) μW at the sample, using an index-matched 1.27 NA water-immersion objective.

Owing to the high axial localization precision offered by measuring directly Φ^+_{FWM} (without involving the cross-polarised FWM field, hence not affected by the NP asymmetry) we measured the axial movement of a single

25 nm radius AuNP while diffusing inside the dense agarose gel, as a proof-of-principle demonstration of single particle tracking. Measurements were performed without beam scanning, by simply tracing over time Φ^{+}_{FWM} while the NP diffuses, and then converting it into the z coordinate, following the dependence $z = (\partial z/\partial\Phi)\Phi^{+}_{\mathrm{FWM}}$ with $\partial z/\partial\Phi = 37\,\mathrm{nm/rad}$, as calibrated in our previous work.[11] Notably, we observed a peculiar behavior of z a function of time, as shown in Fig. 5, indicating that the NP 'jumps' over two pockets in the agarose gel, separated by about 80 nm. In each pocket, the co-circularly polarised FWM amplitude A^{+}_{FWM} (shown in Fig. 5d) is significantly high, indicating that the AuNP remained within a reasonable depth of focus and did not translate significantly out-of-focus laterally, while the time-trace was acquired.

To improve the statistical significance of the analysis, the measurements shown in Fig. 5 on the same NP where sequentially repeated six times and the corresponding histogram of the NP position is shown in Fig. 6. The histogram was fitted as a superposition of two Gaussian distributions. The area of each Gaussian, normalized to the total area, gives the probability to find the NP in each pocket, and was found to be 55% and 45%, i.e. the AuNP has about an equal probability to reside in each pocket.

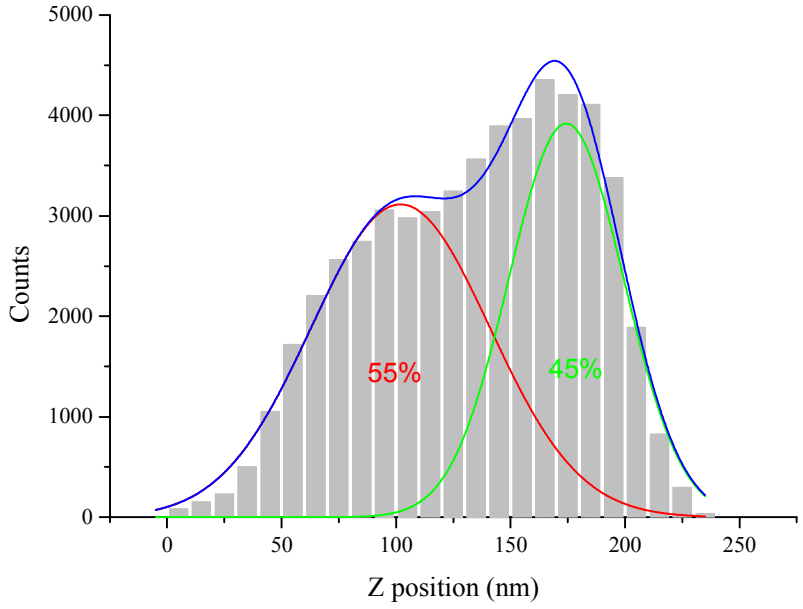

Figure 6. Histogram of the AuNP axial position on the same NP as in Fig. 5, after sequentially acquiring its position via six repetitions of the time-trace. A fit to the histogram as a superposition of two Gaussian distributions is indicated. The area of each Gaussian, normalized to the total area, gives the probability to find the NP in each pocket, and is 55% and 45%, as indicated.

To gain further insights on the type of NP diffusion, we evaluated the temporal autocorrelation function of the axial position, defined as $G(\tau) = \frac{<\delta z(t)\delta z(t+\tau)>}{<z(t)>^2} = \frac{<z(t)z(t+\tau)>}{<z(t)>^2} - 1$, where $\delta z(t) = z(t) - < z(t) >$ and $<>$ denotes the time average. $G(\tau)$ measures how the average correlation between $z(t)$ at two time points t and $t+\tau$ falls off as the time interval τ between the two points increases; the poorer is the correlation, the lower is the value of $G(\tau)$. In essence, a plot of $G(\tau)$ as a function of τ gives us quantitative information about the time scale of the fluctuations in $z(t)$. This analysis is commonly applied in fluorescence correlation spectroscopy, where fluctuations in the fluorescence intensity are measured for fluorescent molecules diffusing into and out of the focal volume, and their autocorrelation function is evaluated.[14]

The more $z(t)$ fluctuates on average between times t and $t+\tau$, the poorer the average correlation will be. Therefore, for values of τ that are much longer than the average time scale of the fluctuations, $G(\tau)$ will fall to zero. Conversely, for values of τ that are much shorter than the time scale of the fluctuations in $z(t)$, so that on average $z(t)$ does not fluctuate (change) significantly between times t and $t+\tau$, the correlation between $z(t)$ and $z(t+\tau)$ will be very high, and $G(\tau)$ will approach its maximum value. $G(\tau)$ for the measured

time-trace $z(t)$ analyzed in Fig. 6 is shown in Fig. 7. We see two ranges over which $G(\tau)$ changes rapidly as a function of τ, indicating that there are two types of fluctuations in the signal, occurring on different time scales. We can reproduce the observed behavior using the functions shown as green and magenta curves in Fig. 7. The green curve is a superposition of an initial fast exponential decay followed by a Gaussian decay, namely: $G(\tau) = G_1 e^{-(\tau/t_1)} + G_2 e^{-(\tau/t_2)^2}$, with $t_1 = 3\,\text{ms}$ and $t_2 = 2.5\,\text{s}$. The magenta curve is a superposition of two inverse polynomial functions, namely: $G(\tau) = G_1/(1 + (\tau/t_1)^2) + G_2/(1 + (\tau/t_2)^{2.8})$ with $t_1 = 2.7\,\text{ms}$ and $t_2 = 2.1\,\text{s}$. A more in depth understanding of the functional dependence of $G(\tau)$, and associated diffusion model, is beyond the scope of this work and will be the subject of future studies, but, in essence, we see two characteristic time constants for the average time scale of the $z(t)$ fluctuations, one in the $\sim 3\,\text{ms}$ time scale and the second one in the $\sim 2\,\text{s}$ time scale. We suggest that $t_1 \sim 3\,\text{ms}$ reflects the time constant of the fast NP motion inside a single agarose gel pocket, while $t_2 \sim 2\,\text{s}$ is related to the time scale over which the NP jumps across the two pockets.

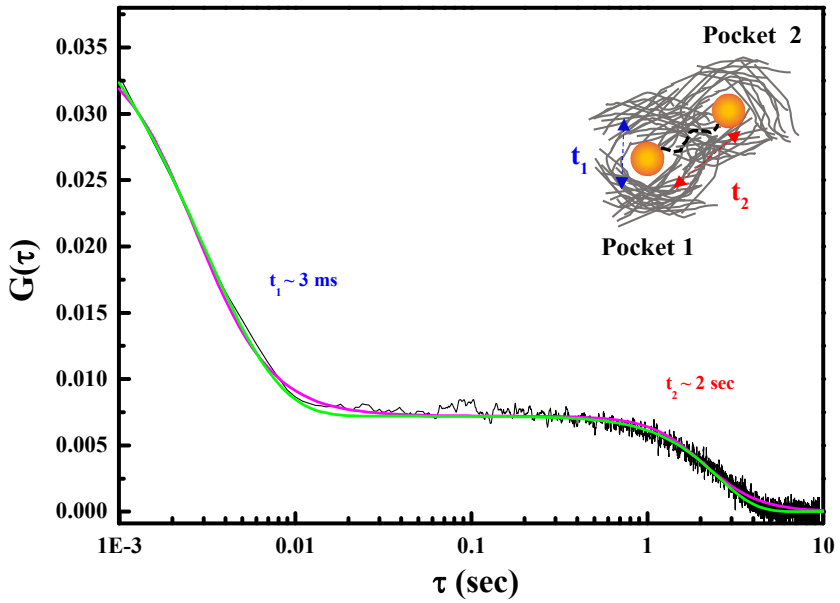

Figure 7. Autocorrelation function of the AuNP axial position on the same NP as in Fig. 6. The green curve is a superposition of an initial fast exponential decay followed by a Gaussian decay . The magenta curve is a superposition of two inverse polynomial functions (see text). Two characteristic time constants are deduced for the average time scale of the $z(t)$ fluctuations: $t_1 \sim 3\,\text{ms}$ and $t_2 \sim 2\,\text{s}$. The inset is a schematic of the proposed NP motion, where $t_1 \sim 3\,\text{ms}$ is the time constant of the fast NP motion inside an agarose gel pocket, while $t_2 \sim 2\,\text{s}$ represents the time scale over which the NP jumps across the two pockets.

5. CONCLUSIONS

In conclusion, we have shown our four-wave mixing interferometry technique, whereby single non-fluorescing gold nanoparticles are imaged background-free even inside highly heterogeneous cellular environments, and their position can be determined with nanometric precision in 3D by exploiting the optical vortex field pattern in the focal plane of a high NA objective. The technique is also uniquely sensitive to particle in-plane asymmetries and orientations. Notably, the set-up features simultaneous correlative confocal fluorescence, which opens the prospect to investigate the intracellular fate and integrity of AuNP-labeled-molecule conjugates, by unambiguously visualising the location of AuNPs in a way that was not possible before. A proof-of-principle demonstration of single particle tracking in the axial direction is shown, owing to the high axial localization precision offered by the technique. A single AuNP of 25 nm radius is rapidly tracked over time by measuring the FWM phase with 1 ms acquisition time per point. By analyzing the histogram of the axial coordinate as well as its temporal autocorrelation, we infer that the NP is jumping across two agarose gel pockets separated by about 80 nm, with a

characteristic time constant $t_1 \sim 3\,\mathrm{ms}$ related the NP motion inside a single pocket, and a time constant $t_2 \sim 2\,\mathrm{s}$ related to the time scale over which the NP jumps across the two pockets. Overall, this technique opens the prospect to an unprecedented level of understanding of the intracellular fate of single small AuNPs and their trafficking within complex 3D architectures.

ACKNOWLEDGMENTS

We acknowledge funding from the European Commission, Research Executive Agency (Marie Curie Action 607842 FINON ITN-2013). P.B. acknowledges the Royal Society for her Wolfson Research Merit award (WM140077).

REFERENCES

[1] Fujiwara, T., Ritchie, K., Murakoshi, H., Jacobson, K., and Kusumi, A., "Phospholipids undergo hop diffusion in compartmentalized cell membrane," *The Journal of Cell Biology* **157**, 1071–1081 (2002).

[2] Ueno, H., Nishikawa, S., Iino, R., Tabata, K. V., Sakakihara, S., Yanagida, T., and Noji, H., "Simple dark-field microscopy with nanometer spatial precision and microsecond temporal resolution," *Biophysical Journal* **98**, 2014–2023 (2010).

[3] Gu, Y., Di, X., Sun, W., Wang, G., and Fang, N., "Three-dimensional super-localization and tracking of single gold nanoparticles in cells," *Anal. Chem.* **84**, 4111–4117 (2012).

[4] Ortega-Arroyo, J. and Kukura, P., "Interferometric scattering microscopy (iscat): new frontiers in ultrafast and ultrasensitive optical microscopy," *Phys. Chem. Chem. Phys.* **14**, 15625–15636 (2012).

[5] Lasne, D., Blab, G. A., Berciaud, S., Heine, M., Groc, L., Choquet, D., Cognet, L., and Lounis, B., "Single nanoparticle photothermal tracking (snapt) of 5-nm gold beads in live cells," *Biophysical J.* **91**, 4598–4604 (2006).

[6] Manzo, C. and Garcia-Parajo, M. F., "A review of progress in single particle tracking: from methods to biophysical insights," *Rep. Prog. Phys.* **78**, 124601 (2015).

[7] Masia, F., Langbein, W., Watson, P., and Borri, P., "Resonant four-wave mixing of gold nanoparticles for three-dimensional cell microscopy," *Opt. Lett.* **34**, 1816–1818 (2009).

[8] Borri, P., Langbein, W., and Masia, F., "Surface plasmon four-wave mixing microscopy," US 8817261 B2; EP 2373980 B1(2010).

[9] Masia, F., Langbein, W., and Borri, P., "Measurement of the dynamics of plasmons inside individual gold nanoparticles using a femtosecond phase-resolved microscope," *Phys. Rev. B* **85**, 235403 (2012).

[10] Masia, F., Langbein, W., and Borri, P., "Polarization-resolved ultrafast dynamics of the complex polarizability in single gold nanoparticles," *Phys. Chem. Chem. Phys.* **15**, 4226–4232 (2013).

[11] Zoriniants, G., Masia, F., Giannakopoulou, N., Langbein, W., and Borri, P., "Background-free 3d nanometric localization and sub-nm asymmetry detection of single plasmonic nanoparticles by four-wave mixing interferometry with optical vortices," *Phys. Rev. X* **7**, 041022 (2017).

[12] Langbein, W., Regan, D., Pope, I., and Borri, P., "Heterodyne dual-polarization epi-detected cars microscopy for chemical and topographic imaging of interfaces," *APL Photonics* **3**, 092402 (2018).

[13] Tortorella, S. and Karagiannis, T. C., "Transferrin receptor-mediated endocytosis: A useful target for cancer therapy," *J. Membrane Biol.* **247**, 291–307 (2014).

[14] Bacia, K. and Schwille, P., "A dynamic view of cellular processes by in vivo fluorescence auto- and cross-correlation spectroscopy," *Methods* **29**, 74–85 (2003).